Title
2D and 3D simulations of static response of a geosynthetic reinforced soil bridge abutment

Journal
Geosynthetics International, 29(5)

ISSN
1072-6349

Authors
Zheng, Y
Guo, W
Fox, PJ
et al.

Publication Date
2022-10-01

DOI
10.1680/jgein.21.00044

Peer reviewed

2D and 3D simulations of static response of a geosynthetic reinforced soil bridge abutment

---

Yewei Zheng [a, *], Wenhao Guo [b], Patrick J. Fox [c], and John S. McCartney [d]

[a] *Professor, School of Civil Engineering, Wuhan University, Wuhan, Hubei, 430072, China; E-mail: yzheng@whu.edu.cn; ORCID Number: 0000-0001-9038-4113 (* corresponding author)*

[b] *Ph.D. Candidate, School of Civil Engineering, Wuhan University, Wuhan, Hubei, 430072, China; E-mail: guowenhao@whu.edu.cn; ORCID Number: 0000-0003-4695-3934*

[c] *Shaw Professor and Head, Department of Civil and Environmental Engineering, Pennsylvania State University, University Park, PA 16802, USA; E-mail: pjfox@engr.psu.edu; ORCID Number: 0000-0001-7279-3490*

[d] *Professor and Chair, Department of Structural Engineering, University of California San Diego, La Jolla, CA, 92093-0085, USA; E-mail: mccartney@ucsd.edu; ORCID Number: 0000-0003-2109-0378*

ABSTRACT: This paper presents two-dimensional (2D) and three-dimensional (3D) numerical simulations of a half-scale geosynthetic reinforced soil (GRS) bridge abutment during construction and bridge load application. The backfill soil was characterized using a nonlinear elasto-plastic model that incorporates a hyperbolic stress-strain relationship and the Mohr-Coulomb failure criterion. Geogrid reinforcements were characterized using linearly elastic elements with orthotropic behavior. Various interfaces were included to simulate the interaction between the abutment components. Results from the 2D and 3D simulations are compared with physical model test measurements from the longitudinal and transverse sections of a GRS bridge abutment. Facing displacements and bridge seat settlements for the 2D and 3D simulations agree well with measured values, with the 2D simulated values larger than the 3D simulated values due to boundary condition effects. Results from the 3D simulation are in reasonable agreement with measurements from the longitudinal and transverse sections. The 2D simulation can also reasonably capture the static response of GRS bridge abutments and is generally more conservative than the 3D simulation.

KEYWORDS: Geosynthetics, Geosynthetic reinforced soil, Bridge abutment, Numerical simulation, Three-dimensional; Two-dimensional.

1. Introduction

Geosynthetic reinforced soil (GRS) bridge abutments are becoming widely used in transportation infrastructure. Several case histories of in-service GRS bridge abutments have been reported in the literature and indicate good performance in terms of facing displacements and bridge seat settlements (Abu-Hejleh et al. 2002; Adams et al. 2011; Saghebfar et al. 2017; Talebi et al. 2017; Gebremariam et al. 2020a, 2020b). Field and laboratory loading tests have also been conducted on GRS piers and abutments and yielded important findings (e.g., Wu et al. 2001, 2006; Pham 2009; Nicks et al. 2013, 2016; Adams et al. 2014; Iwamoto et al. 2015; Xiao et al. 2016; Xu et al. 2019; Zheng et al. 2019a, 2019b). Such experimental studies are typically time-consuming, labor intensive and costly.

Numerical modeling studies, when properly validated, can be used to effectively compliment and augment experimental research. Most numerical studies of GRS bridge piers and abutments are two-dimensional (2D) and predict relatively small magnitudes of facing displacements and bridge seat settlements under service load conditions (e.g., Helwany et al. 2003, 2007; Ambauen et al. 2015; Leshchinsky and Xie 2015; Kaya 2016; Zheng and Fox 2016, 2017; Ardah et al. 2017; Zheng et al. 2018a; Shen et al. 2020). Corresponding parametric evaluations from these studies indicate that the relative compaction of backfill soil, reinforcement vertical spacing, reinforcement tensile stiffness, and bridge load have the most significant effects on the performance of GRS bridge abutments.

Although these 2D numerical studies provide important insights into the performance of GRS piers and abutments, three-dimensional (3D) numerical modeling is needed to accurately capture the stress paths and boundary conditions for these systems. Zheng et al. (2018b) validated a 3D numerical model for GRS mini-piers under service load conditions using a nonlinear elasto-plastic model that incorporated a hyperbolic stress-strain relationship for the backfill soil and a linear elastic orthotropic model for the geotextile reinforcement. Simulation results indicate that backfill soil friction angle, backfill soil apparent cohesion, reinforcement spacing, and reinforcement stiffness have important effects on settlements and facing displacements under service load conditions. Rong et al. (2017) conducted a 3D numerical simulation for a GRS bridge abutment and found that the application of bridge load produced multi-directional deformations, including outward displacements for the front wall facing and smaller outward displacements for the side wall facings. Additional investigations that consider 3D effects are needed to better understand the static response of GRS bridge abutments in both the longitudinal and transverse directions.

Research on the comparison of 2D and 3D numerical modeling results for GRS piers and abutments is limited. Abu-Farsakh et al. (2018) conducted both 2D and 3D numerical simulations for a GRS-IBS abutment that included comparisons with field measurements. Results indicate that facing displacements for 3D simulations were slightly smaller than those for the 2D simulations, both of which generally agreed well with the field measurements. Shen et al. (2019) conducted 2D and 3D numerical simulations for GRS mini-piers using a linearly elastic-perfectly plastic soil model and a linear elastic reinforcement model. Simulation results indicate that 2D plane strain conditions are more conservative than 3D conditions because lateral facing displacements are permitted for opposite sides of the mini-piers in 2D but for all four sides in 3D. In addition, the use of plane strain conditions requires the assumption of frictionless side boundaries and do not account for mechanical interlocking at the corner of the GRS bridge abutment facings in 3D conditions.

This paper presents a numerical investigation of a half-scale GRS bridge abutment specimen during construction and bridge load application. 2D and 3D numerical simulations were conducted considering the nonlinear behavior of backfill soil, orthotropic behavior of the geogrid in the machine and cross-machine directions, various interfaces between different components, and staged construction. Simulation results are compared with experimental measurements for the longitudinal and transverse sections of a GRS bridge abutment to better understand the multi-directional response of this system under static loading.

2. Numerical model

The finite difference program *FLAC3D Version 5.0* (Itasca Consulting Group 2015) was used for the current investigation to simulate the static response of a half-scale GRS bridge abutment specimen as measured from a physical model test. Considering a length scaling factor of 2, the half-scale GRS bridge abutment specimen corresponds to a prototype GRS bridge abutment with a clearance height of 4.5 m, which satisfies Federal Highway Administration (FHWA) requirements (Zheng et al. 2019a). A 3D numerical model was developed to simulate the GRS bridge abutment system, and a 2D numerical model was developed to simulate a plane strain slice of the system in the longitudinal direction. The details of the experimental program, including scaling relationships, specimen configuration, material properties, construction procedures, and instrumentation, are reported by Zheng et al. (2018c, 2019a).

2.1. Model configuration and instrumentation

The 3D model for the GRS bridge abutment developed using *FLAC3D* is shown in Figure 1. A bridge beam rests on a GRS bridge abutment with a concrete bridge seat at one end and on a concrete support wall at the other end. The GRS bridge abutment specimen includes three modular block wall facings, including one front wall facing (perpendicular to the bridge beam) and two side wall facings (parallel to the bridge beam), and the back of the specimen is supported by a reaction wall. The bottom boundary of the model was fixed in the x, y, and z directions. All four lateral boundaries were fixed in the direction perpendicular to the plane boundary and free to displace in all directions parallel to the boundary.

Cross-sections of the GRS bridge abutment model in the longitudinal and transverse directions are shown in Figures 1(b) and 1(c), respectively. The 2.7 m-high GRS bridge abutment consists of a 2.1 m-high lower GRS fill and a 0.6 m-high upper GRS fill. The lower GRS fill has fourteen 0.15 m-thick soil lifts, with each lift including reinforcement layers in both the longitudinal and transverse directions. Reinforcement layers perpendicular to the diagram are shown as dashed lines in Figure 1. The transverse reinforcement layers and side wall facing blocks for each lift are offset by 25 mm vertically from the longitudinal reinforcement layers and front wall facing blocks. The reinforcement layers were placed between facing blocks with frictional connections. The upper GRS fill consists of four 0.15 m-thick soil lifts with reinforcement layers only in the transverse direction. The total weight of the bridge seat and bridge beam (including dead weights) produces an average applied surcharge stress of 66 kPa on the lower GRS fill. The soil used for the foundation layer and GRS bridge abutment specimen was a well-graded angular sand with no gravel and a low fines content, and the reinforcement was a uniaxial high-density polyethylene (HDPE) geogrid (Zheng 2018c, 2019a). Instrumentation for the abutment specimen is shown in Figure 2 for top view, longitudinal section L1, and transverse section T1.

In addition to the 3D numerical model, a 2D numerical model was simulated using *FLAC3D* for the longitudinal centerline section L1. *FLAC3D* was used to ensure consistency between the 2D and 3D models with regard to the modeling approach and constitutive models. The 2D longitudinal model has a thickness of 0.3 m in the third dimension (equivalent to the width of one facing block) and was developed for plane strain conditions. Consistent with the 3D model, the average applied surcharge stress on the lower GRS fill is 66 kPa for the 2D model.

2.2. Soil

The foundation soil and backfill soil were the same in this study. The soil was modeled as a nonlinear elasto-plastic material with the Duncan-Chang hyperbolic stress-strain relationship (Duncan et al. 1980) and the Mohr-Coulomb failure criterion. The soil model accounts for nonlinear behavior and has been used to simulate the static response of GRS bridge abutments under service load conditions (Zheng and Fox 2016, 2017). The tangent elastic modulus E_t, unloading-reloading modulus E_{ur}, bulk modulus B, and tangent Poisson's ratio ν_t are expressed as (Duncan et al. 1980):

$$E_t = \left[1 - \frac{R_f(1-\sin\phi')(\sigma_1' - \sigma_3')}{2c'\cos\phi' + 2\sigma_3'\sin\phi'}\right]^2 K p_a \left(\frac{\sigma_3'}{p_a}\right)^n \quad (1)$$

$$E_{ur} = K_{ur} p_a \left(\frac{\sigma_3'}{p_a}\right)^n \quad (2)$$

$$B = K_b p_a \left(\frac{\sigma_3'}{p_a}\right)^m \quad (3)$$

$$\nu_t = \frac{1}{2} - \frac{E_t}{6B} \quad (4)$$

where σ_1' and σ_3' = major and minor principal effective stresses; ϕ' = friction angle; c' = cohesion; R_f = failure ratio; K = elastic modulus number; n = elastic modulus exponent; p_a =

atmospheric pressure (101.3 kPa); K_{ur} = unloading-reloading modulus number; K_b = bulk modulus number; m = bulk modulus exponent; and ν_t has a range of 0 to 0.49.

Soil parameters were calibrated using measured data from consolidated-drained triaxial compression tests on dry sand specimens compacted to a relative density of 70%, which corresponds to the target compaction density during construction of the GRS bridge abutment specimen (Zheng et al. 2019a). Comparison of simulated and measured results is shown in Figure 3 and indicates accurate reproduction of nonlinear stress-strain behavior up to the peak shear strength. The sand has a peak friction angle of ϕ'_p = 51.3°. The post-peak strain softening response at high axial strain is not captured by the model, and the model does not capture the dilation behavior observed in the triaxial tests at high axial strains. However, these are not expected to significantly affect the findings of the current study that focuses on service load conditions (Zheng et al. 2018a). Based on the measured gravimetric water content for each lift during construction, the apparent cohesion was calculated using the soil-water retention curve (SWRC) reported by Zheng et al. (2019a) and the suction stress concept of Lu et al. (2010). Calculated values of apparent cohesion are relatively uniform with elevation and have an average of 2 kPa. A summary of soil parameters is presented in Table 1.

2.3. Reinforcement

The geogrid reinforcement was modeled using linearly elastic geogrid elements with orthotropic behavior to account for different properties in the machine direction (MD) and cross-machine direction (CMD). As such, different values of tensile stiffness were assigned for MD and CMD according to results from tensile tests (ASTM D6637). For the physical model test, the reinforcement strain level was approximately 0.15% and the elapsed time for construction was approximately 7 days (168 hours) for the GRS bridge abutment specimen (Zheng et al. 2019a). According to the data sets of uniaxial HDPE geogrid reported by Bathurst and Naftchali (2021), the creep stiffness for strain level of 0.15% and elapsed time of 168 hours is approximately the same as the secant stiffness at 5% strain from constant rate-of-strain test at 10% strain/min. Therefore, the secant stiffness at 5% strain $J_{5\%}$ = 380 kN/m in the MD and $J_{5\%}$ = 80 kN/m in the CMD from constant rate-of-strain tensile tests were selected as the reinforcement stiffness values. The elastic modulus E_r was calculated using $J_{5\%}$ as:

$$E_r = J_{5\%} / t_r \quad (5)$$

where t_r is the geogrid thickness. The geogrid has t_r = 1 mm, E_r = 380 MPa in the MD, and E_r = 80 MPa in the CMD.

2.4. Structure components

The modular facing blocks, bridge seat, support wall, reaction wall, and shaking table were modeled as linearly elastic materials with unit weight γ = 23.5 kN/m^3, elastic modulus E = 20 GPa, and Poisson's ratio ν = 0.2. The bridge beam was modeled as an elastic solid block with E = 20 GPa and ν = 0.2. Considering the total weight of concrete beam and additional dead weights, the equivalent unit weight of this solid block γ_b = 37.8 kN/m^3, which produced an average applied surcharge stress q_v = 66 kPa on the lower GRS fill. Similarly, the equivalent unit weight for one slice of the solid block with a thickness of 0.3 m was 27.1 kN/m^3 for the 2D longitudinal model to produce the same value of q_v = 66 kPa.

2.5. Interfaces

The interaction between different components of the GRS bridge abutment system was modeled through interfaces, in which the interface shear strength is defined using interface friction angle δ_i' and adhesion c_i'. Soil interface shear strength parameters (e.g., soil-geogrid, soil-block, and soil-bridge seat) are characterized using a reduction factor RF defined as:

$$RF = \frac{\tan\delta_i'}{\tan\phi_p'} = \frac{c_i'}{c'} \quad (6)$$

The shear strength parameters for soil interfaces, block-geogrid interfaces, block-block interfaces, and bridge beam-bridge seat interfaces were selected according to data from references, as summarized in Table 2. The values of normal stiffness k_n and shear stiffness k_s for the interfaces were determined according to the *FLAC* Manual (Itasca Consulting Group 2015).

2.6. Modeling procedures

The 3D numerical model for the GRS bridge abutment system was constructed in stages. The support structures, including shaking table, reaction wall, and support wall were first resolved to equilibrium under gravitational forces. The foundation soil layer then was placed on the shaking table and the lower GRS wall was constructed in fourteen layers, with each layer consisting of one lift of soil, one course of facing blocks (three sides), geogrid layers in both the longitudinal and transverse directions, and interfaces between different components. A temporary uniform vertical surcharge stress of 8 kPa was applied to the top surface of each soil lift, and then removed prior to placement of the next lift to simulate the effects of backfill soil compaction. This modeling approach for soil compaction has been widely used and validated in many previous studies (e.g., Hatami and Bathurst 2006; Guler et al. 2007; Huang et al. 2010; Yu et al, 2016; Zheng and Fox 2017). Once the lower GRS wall was completed, the bridge seat was placed on top of the fill, and the upper GRS fill was similarly constructed in lifts with only transverse reinforcement layers connected to side wall facings. The bridge beam then was placed on the bridge seat and support wall. For each construction stage and soil layer, the numerical model was resolved to equilibrium under gravitational forces. A sensitivity analysis also was conducted to investigate the effect of mesh size on the simulation results. Considering the computational accuracy and efficiency, a total of 10,297 elements was selected for the 3D numerical model, with mesh elements shown in Figures 1(b) and 1(c). The 2D longitudinal model was constructed in stages in the same manner and contained 791 elements.

3. Simulation results

Results from the 3D numerical simulation are presented for the instrumented longitudinal section L1 and transverse section T1 (Figure 2) of the GRS bridge abutment specimen, and results from the 2D numerical simulation also are presented for comparison. Simulated and measured results, including wall facing displacements, bridge seat settlements, soil stresses, and reinforcement tensile strains and tensile forces, are evaluated after construction of the lower GRS wall (Stage 1), after placement of the bridge seat and construction of the upper GRS fill (Stage 2), and after placement of the bridge beam (Stage 3). Outward displacements for the front wall and side wall facings and downward displacements (i.e., settlements) for the bridge seat are defined as positive.

3.1. Facing displacements

Profiles of wall facing displacement for the longitudinal section L1 (i.e., front wall) and the transverse section T1 (i.e., west side wall) after each stage of construction are shown in Figure 4, and the maximum value from each profile is presented in Figure 5. For the longitudinal section, measured facing displacements for section L1 generally increase with elevation, with maximum values of 2.3 mm for Stage 1 and 3.2 mm for Stage 3. 2D and 3D simulations show similar profile shapes, with displacements increasing from the bottom of the wall, reaching the maximum near the mid-height, and then decreasing toward the top. The maximum facing displacement for the 3D simulation increases from 1.8 mm for Stage 1 to 2.8 mm for Stage 3, and the corresponding values for 2D simulation are slightly larger and the maximum value increases from 2.0 mm to 3.6 mm. The prediction deviations, defined as the difference between the simulated and measured values divided by the measured value, are 22% for Stage 1 and 12% for Stage 3.

In general, facing displacements for the longitudinal section in both the 2D and 3D simulations are in reasonable agreement with measured displacements, with the 3D simulated values slightly smaller than the measured values and the 2D simulated values mostly larger. This suggests that the 2D simulation is more conservative than the 3D simulation in terms of facing displacements, which is consistent with the observations reported by Shen et al. (2019). This conservatism is explained by boundary conditions, in which outward displacements were permitted on three sides (one front wall facing and two side wall facings) for the 3D simulation, but only on one side (front wall facing) for the 2D simulation. In addition, the soil shear stresses developed between adjacent longitudinal slices in the 3D model could restrict the relative movements, while frictionless side boundaries were assumed for the 2D model.

In Figure 4(b) for the transverse section, the 3D simulated facing displacement profiles for are in good agreement with measured displacement profiles. Simulated and measured maximum facing displacements are close and both occur at the mid-height of the wall with prediction deviations ranging from 5% to 23% for all three stages. The simulated maximum displacement for transverse section T1 is 1.3 mm for Stage 1 and 2.0 mm for Stage 3, which are smaller than corresponding maximum values of 1.9 mm and 2.8 mm for longitudinal section L1. In general, simulated facing displacements for the longitudinal and transverse sections are in reasonable agreement with measurements with respect to both magnitude and trend.

3.2. Bridge seat settlements

Measured settlements at the four top corners of bridge seat due to placement of bridge beam (i.e., difference from Stage 2 to Stage 3) are shown in Figure 6. Measured values are 3.4 mm, 0.7 mm, and 2.9 mm at the NW, NE, and SW corners, respectively. The string potentiometer on the SE corner malfunctioned for this stage, as reported by Zheng et al. (2019a), and the corresponding measurement is unavailable. The measured settlement of 0.7 mm at the NE corner is small and likely reflects tilting of the bridge seat toward the west during placement of the bridge beam (Zheng et al. 2019a) due to initial imperfect contact (i.e., gap) between the bridge seat and top of reinforced soil (Gebremariam et al. 2020a).

Figure 6 also provides settlements from the 3D and 2D simulations. Settlements on the north side (NW and NE corners) in both the 3D and 2D simulations are equal and settlements on the south side (SW and SE corners) are equal. For the 3D simulation, the settlements of 3.8 mm on the north side (NW and NE) are slightly larger than the value of 3.5 mm on the south side (SW and SE), which indicates tilting of the bridge seat towards north under the bridge surcharge stress. The 3D simulated average bridge seat settlement of the four corners is 3.6 mm, which corresponds to a vertical strain of 0.17% for the 2.1 m-high lower GRS fill. Settlements on the north and south sides for the 2D simulation are 3.9 mm and 3.6 mm, which are slightly larger than the values for the 3D simulation. In general, simulated settlements on the west side of the bridge seat (NW and SW) for 2D and 3D simulations are in good agreement with the corresponding measured values. The 2D and 3D simulations provided reasonable estimates of the average bridge seat settlements.

3.3. Soil stresses

Profiles of vertical soil stress for the longitudinal section and Stages 1 and 3 are shown in Figure 7. Vertical stress profiles calculated using the AASHTO (2020) method also are shown for comparison, in which values for Stage 1 were calculated using soil self-weight and values for Stage 3 were calculated using soil self-weight plus a fraction of the applied surcharge stress obtained from a 2:1 stress distribution. For Stage 1, vertical soil stresses for both 2D and 3D simulations increase approximately linearly with depth and are in close agreement with the calculated AASHTO (2020) values. Measured vertical soil stresses are in good agreement with the simulated values near the top but deviate significantly with increasing depth. This is attributed to the friction developed at the back of facing blocks and partial support of backfill soil weight from reinforcement near the facing, similar to the findings of Runser et al. (2001) for a steel-reinforced soil wall. However, these effects are not well captured in the simulations, because the approach to model the soil compaction effect using an equivalent uniform surcharge stress does not accurately simulate the local differential settlements between the facing blocks and backfill soil.

Corresponding vertical stresses for Stage 3 are presented in Figure 7(b) and show similar profile shapes, with the 2D values generally larger than the 3D values. The vertical stress profile for the 3D simulation most closely matches the measured profile, with the simulated values smaller near the top and larger near the bottom. The differences between the 3D simulated and measured stresses near the bottom are close to the differences for Stage 1. Profiles of incremental vertical stress from Stage 1 to Stage 3 are shown in Figure 7(c). Incremental stresses for the 3D simulation are in better agreement with measurements. The 2D and 3D simulated incremental vertical soil stresses are smaller than calculated incremental values using the AASHTO (2020) method, which indicates that the AASHTO (2020) method generally is conservative for applied surcharge stress.

Corresponding profiles of lateral (i.e., horizontal) soil stress behind the front wall facing are shown in Figure 8, along with calculated values obtained using the AASHTO (2020) vertical stress profiles in Figure 7 multiplied by the Rankine active earth pressure coefficient K_a (= 0.12). For Stage 1, with increasing depth, the 3D simulated lateral stresses are generally small (less than 2 kPa) at the top and then increase significantly toward the bottom of the wall. The 3D and 2D simulations show much larger stresses than the measured and calculated AASHTO values near the bottom, which is attributed to the large toe restraint due to friction developed between the lowermost facing block and foundation soil. Lateral soil stresses for the 3D simulation are generally smaller than those for the 2D simulation, especially near the mid-height of the wall because soil deformations in the out-of-plane direction were restricted for the 2D simulation.

For Stage 3, shown in Figure 8(b), the 3D simulated lateral soil stresses are generally in good agreement with measured values and smaller than the calculated AASHTO (2020) values except near the bottom of the wall. The 2D simulated lateral stresses increase significantly with depth, with much larger values than the 3D simulation due to constraints of the plane strain conditions. Profiles of incremental lateral soil stress from Stage 1 to Stage 3 are shown in Figure 8(c). Incremental stresses for the 3D simulation are slightly larger than the measured values but much smaller than the calculated AASHTO (2020) values, which again indicates that the AASHTO (2020) method is conservative.

3.4. Reinforcement tensile strains

Distributions of reinforcement tensile strains are shown in Figure 9. For the longitudinal section, shown in Figure 9(a), tensile strains from the 3D simulation for Stages 1 and 2 are much larger in the lower and mid-height reinforcement layers than in the upper layers. For Stage 3, tensile strains increase substantially due to placement of the bridge beam, especially in the upper layers under the bridge seat. Tensile strains for the 3D simulation are smaller than for the 2D simulated values at the end of each construction stage, especially near the facing connections. The simulated maximum strain in each reinforcement layer occurs under the bridge seat (i.e, x = 0.4 m to 0.7 m) for the 3D simulation and near the facing connections for the 2D simulation. Measured maximum values of reinforcement tensile strain occur near the facing connections in lower layers 1, 4, and 7, and under the bridge seat in upper layers 10 and 13. In general, reinforcement tensile strains for the 3D simulation are in good agreement with the measured values except for some deviations near the facing connections for the mid-height layers.

Reinforcement tensile strains for the transverse section are shown in Figure 9(b). The maximum strain in each reinforcement layer from the 3D simulation occurs under the bridge seat for all three stages. The 3D simulated values are close to the measured values for Stages 1 and 2, but smaller in layers 7 and 13 for Stage 3, which likely results from tilting of the bridge seat toward the west side during construction (Zheng et al. 2019a).

3.5. Reinforcement tensile forces

Profiles of maximum tensile forces in each reinforcement layer for the longitudinal and transverse sections are shown in Figure 10. The measured reinforcement tensile forces were converted from the measured strains using a constant stiffness value of 380 kN/m. Maximum tensile forces calculated from the Simplified Method and the Stiffness Method from AASHTO (2020) using the soil peak friction angle of 51.3°also are presented for comparison. For Stage 1, shown in Figure 10(a), simulated maximum reinforcement tensile force profiles for sections L1 and T1 in the 3D simulation are nearly the same. Maximum tensile forces first increase linearly with depth from the top of the wall, reach the highest value of approximately 0.2 kN/m at z = 0.75 m, and then decrease slightly toward the bottom. The 3D simulated maximum tensile forces for sections L1 and T1 are smaller than the measured values. The measured highest tensile forces for sections L1 and T1 are 0.43 kN/m and 0.33 kN/m, respectively. The 2D simulated maximum tensile forces are generally larger than the measured forces with the highest value of 0.5 kN/m at z = 1.05 m. Calculated maximum tensile forces using the Stiffness Method are generally close to the 3D simulated values, but are smaller than the measured values. Calculated forces using the Simplified Method are larger than the 3D simulated values and are generally close to the 2D simulated values and measurements except near the bottom.

For Stage 3, shown in Figure 10(b), the 3D simulated maximum tensile forces increased significantly in the upper layers due to application of bridge surcharge stress. The 3D simulated maximum force profiles for sections L1 and T1 are relatively uniform, with the tensile forces for L1 slightly larger than those for T1 near the top of the wall, and the highest values are 0.43 kN/m and 0.32 kN/m, respectively. Similar to Stage 1, the 3D simulated maximum tensile forces are generally smaller than the measured values. Maximum tensile forces from the 2D simulation for section L1 are much larger than for the 3D simulation and measurements, and the highest value is 0.85 kN/m. Calculated maximum tensile forces using the Stiffness Method generally increase with elevation and are larger than the 3D simulated values and measurements, while the Simplified Method shows even larger tensile forces in the lower section of the abutment. In general, the 2D simulation is more conservative than the 3D simulation in terms of maximum tensile forces, with the 3D simulation underestimating the measured maximum tensile forces and the 2D simulation overestimating the measured values. In addition, both the Simplified Method and Stiffness Method overestimate the maximum tensile forces, with the Simplified Method having larger overestimations.

4. Conclusions

This paper presents experimental measurements and two-dimensional (2D) and three-dimensional (3D) numerical simulations for a half-scale geosynthetic reinforced soil (GRS) bridge abutment specimen under static loading. The backfill soil was characterized using a nonlinear elasto-plastic model that incorporates a hyperbolic stress-strain relationship and the Mohr-Coulomb failure criterion. Geogrid reinforcements were characterized using linearly elastic elements with orthotropic behavior. Various interfaces were included to simulate the interaction between different GRS bridge abutment components. Results from the 2D and 3D simulations were compared with measurements from instrumented sections in the longitudinal and transverse directions. The following conclusions are reached for the conditions of the study:

1. Facing displacements and bridge seat settlements for the 2D and 3D simulations are in reasonable agreement with measurements, with the 2D simulated values larger than the 3D simulated values. The 2D simulation is more conservative than the 3D simulation in terms of deformations because of boundary condition effects, in which outward

displacements were permitted on three sides for the 3D simulation, but only on one side for the 2D simulation. In addition, the soil shear stresses developed between adjacent longitudinal slices in the 3D model could restrict the relative movements, while frictionless side boundaries were assumed for the 2D model.

2. Incremental vertical and lateral soil stresses due to the applied surcharge stress for the 3D simulation are in reasonable agreement with measured values. In general, the AASHTO (2020) method for the calculation of incremental vertical and lateral soil stress under the applied surcharge stress is conservative.
3. The maximum tensile strain in each reinforcement layer for the 3D simulation occurs under the bridge seat in the longitudinal section. In general, the 3D simulated reinforcement strains are in good agreement with the measured values except for some deviations near the facing connections in the mid-height layers, and generally are smaller than corresponding strains from the 2D simulation.
4. Profiles of maximum tensile force for sections L1 and T1 in the 3D simulation were nearly uniform with elevation with the highest values near the top of the wall under applied surcharge stress. In general, the 2D simulation is more conservative than the 3D simulation in terms of maximum tensile forces, with the 3D simulation underestimating the measured maximum tensile forces and the 2D simulation overestimating the measured values. In addition, both the Simplified Method and Stiffness Method in AASTHO (2020) overestimate the maximum tensile forces.
5. Results from the 3D numerical simulation are generally in reasonable agreement with measurements from instrumented sections in the longitudinal and transverse directions. The 2D simulation can also reasonably capture the static response of GRS bridge

abutments and generally is more conservative than the 3D simulation.

This study focuses on the 2D and 3D response of a half-scale GRS bridge abutment specimen from physical model test. The abutment specimen is relatively narrow in the out-of-plane direction due to the limitation of construction site conditions. Accordingly, numerical simulations on GRS bridge abutments with realistic geometric conditions are needed to further investigate the 2D and 3D static behavior of GRS bridge abutments. Nonetheless, the comparisons between the simulations and experiments in this study provide useful insights into this problem and show that simulations can effectively predict the static response of GRS bridge abutments for service load conditions.

Acknowledgements

Financial supports for this study provided by the California Department of Transportation (Caltrans) Project 65A0556 and Federal Highway Administration (FHWA) Pooled Fund Project 1892AEA are gratefully acknowledged. This research work is also supported by the National Natural Science Foundation of China under Grant No. 52078392, and the financial support is greatly appreciated.

Notations

Basic SI units are given in parentheses.

B bulk modulus (kPa)

c' apparent cohesion (kPa)

c_i' interface adhesion (kPa)

E elastic modulus (kPa)

E_r elastic modulus for reinforcement (kPa)

E_t tangent elastic modulus (kPa)

E_{ur} unloading-reloading modulus (kPa)

$J_{5\%}$ reinforcement secant stiffness at 5% tensile strain (kN/m)

K elastic modulus number

K_b bulk modulus number

K_{ur} unloading-reloading modulus number

m bulk modulus exponent

n elastic modulus exponent

p_a atmospheric pressure (kPa)

q_v applied surcharge stress on lower GRS fill (kPa)

RF_i reduction factor for soil interface shear strength

R_f failure ratio

t_r thickness of reinforcement (mm)

x distance from front wall facing (m)

y distance from west side wall facing (m)

z elevation above foundation soil (m)

δ_i' interface friction angle (°)

ϕ' friction angle (°)

γ soil unit weight (kN/m^3)

γ_b equivalent unit weight of bridge beam (kN/m^3)

ν Poisson's ratio

ν_t tangent Poisson's ratio

σ_1' major principal effective stress (kPa)

σ_3' major principal effective stress (kPa)

Abbreviations

2D two-dimensional

3D three-dimensional

AASHTO American Association of State Highway and Transportation Officials

CMD cross-machine direction

FHWA Federal Highway Administration

GRS geosynthetic reinforced soil

HDPE uniaxial high-density polyethylene

MD machine direction

NE northeast

NW northwest

SE southeast

SW southwest

SWRC soil water retention curve

References

AASHTO, 2020. *AASHTO LRFD Bridge Design Specifications*. 9th Edition. American Association of State Highway and Transportation Officials, Washington, D.C.

Abu-Farsakh, M., Ardah, A., Voyiadjis, G., 2018. 3D finite element analysis of the geosynthetic reinforced soil-integrated bridge system (GRS-IBS) under different loading conditions, *Transportation Geotechnics*, 15, 70-83.

Abu-Hejleh, N., Zornberg, J.G., Wang, T., Watcharamonthein, J., 2002. Monitored displacements of unique geosynthetic-reinforced soil bridge abutments. *Geosynthetics International*, 9(1), 71-95.

Adams, M., Nicks, J., Stabile, T., Wu, J., Schlatter, W., Hartmann, J., 2011. Geosynthetic Reinforced Soil Integrated Bridge System Synthesis Report. *FHWA-HRT-11-027*. U.S. Department of Transportation.

Adams, M.T., Ooi, P.S., Nicks, J.E., 2014., Mini-pier testing to estimate performance of full-scale geosynthetic reinforced soil bridge abutments. *Geotechnical Testing Journal*, 37(5), 884-894.

Ambauen, S., Leshchinsky, B., Xie, Y., Rayamajhi, D., 2016. Service-state behavior of reinforced soil walls supporting spread footings: a parametric study using finite-element analysis. *Geosynthetics International*, 23(3), 156-170.

Ardah, A., Abu-Farsakh, M., Voyiadjis, G., 2017. Numerical evaluation of the performance of a Geosynthetic Reinforced Soil-Integrated Bridge System (GRS-IBS) under different loading conditions. *Geotextiles and Geomembranes*, 45(6), 558-569.

ASTM D6637-15, 2015. *Standard Test Method for Determining Tensile Properties of Geogrids by the Single or Multi-Rib Tensile Method*, ASTM International.

Bathurst, R.J., Naftchali, F.M., 2021. Geosynthetic reinforcement stiffness for analytical and numerical modelling of reinforced soil structures. Geotextiles and Geomembranes, 49, 921-940.

Caltrans., 1994. Memos to Designers 7-1. California Department of Transportation, Sacramento, CA.

Duncan, J.M., Byrne, P., Wong, K.S., Mabry, P., 1980. Strength, Stress-Strain and Bulk Modulus Parameters for Finite Element Analysis of Stresses and Movements in Soil Masses. Report No. UCB/GT/80-01. University of California, Berkeley, CA.

FLAC3D Version 5.0 [Computer software], 2015. Itasca Consulting Group, Minneapolis, MN.

Gebremariam, F., Tanyu, B.F., Christopher, B., Leshchinsky, D., Han, J., and Zornberg, J.G., 2020a. Evaluation of vertical stress distribution in field monitored GRS-IBS structure. *Geosynthetics International*. DOI:10.1680/jgein.20.00004.

Gebremariam, F., Tanyu, B.F., Christopher, B., Leshchinsky, D., Zornberg, J.G., and Han, J., 2020b. Evaluation of required connection load in GRS-IBS structures under service loads. *Geosynthetics International*. 27(6), 620-634.Guler, E., Hamderi, M. & Demirkan, M. M. (2007). Numerical analysis of reinforced soil-retaining wall structures with cohesive and granular backfills. *Geosynthetics International*, Vol. 14, No. 6, 330–345.

Hatami, K., Bathurst, R.J., 2006. Numerical model for reinforced soil segmental walls under surcharge loading. *Journal of Geotechnical and Geoenvironmental Engineering*, 132(6), 673-684.

Helwany, S.M.B., Wu, J.T.H., Froessl, B., 2003. GRS bridge abutments – an effective means to alleviate bridge approach settlement. *Geotextiles and Geomembranes*, 21(3), 177-196.

Helwany, S.M.B., Wu, J.T.H., Kitsabunnarat, A., 2007. Simulating the behavior of GRS bridge abutments. *Journal of Geotechnical and Geoenvironmental Engineering*, 133(10), 1229-1240.

Huang, B., Bathurst, R. J., Hatami, K. & Allen, T. M. (2010). Influence of toe restraint on reinforced soil segmental walls. *Canadian Geotechnical Journal*, Vol. 47, No. 8, 885-904.

Iwamoto, M.K., Ooi, P.S., Adams, M.T., Nicks, J.E., 2015. Composite properties from instrumented load tests on mini-piers reinforced with geotextiles. *Geotechnical Testing Journal*, 38(4), 397-408.

Kaya, L.H., 2016. *Numerical load testing of a geosynthetic reinforced soil*. Master Thesis. University of Hawaii, Manoa.

Leshchinsky, B., and Xie, Y. (2015). "MSE walls as bridge abutments: Optimal reinforcement density." *Geotextiles and Geomembranes*, 43(2), 128-138.

Ling, H.I., Yang, S., Leshchinsky, D., Liu, H., Burke, C., 2010. Finite-element simulations of full-scale modular-block reinforced soil retaining walls under earthquake loading. *Journal of Engineering Mechanics*, 136(5), 653-661.

Lu, N., Godt, J.W., Wu, D.T., 2010. A closed-form equation for effective stress in unsaturated soil. *Water Resources Research*, 46, W05515, 10.1029/2009WR008646.

Nicks, J.E., Adams, M.T., Ooi, P.S.K., Stabile, T., 2013. Geosynthetic reinforced soil performance testing – axial load deformation relationships. *FHWA-HRT-13-066*, U.S. DOT, Washington, D.C.

Nicks, J.E., Esmaili, D., Adams, M.T., 2016. Deformations of geosynthetic reinforced soil under bridge service loads. *Geotextiles and Geomembranes*, 44(4), 641-653.

Pham, T.Q., 2009. *Investigating composite behavior of geosynthetic reinforced soil (GRS) mass*. Ph.D. Dissertation, University of Colorado, Denver.

Rong, W., Zheng, Y., McCartney, J.S., Fox, P.J., 2017. 3D deformation behavior of geosynthetic reinforced soil bridge abutments. *Geotechnical Frontiers 2017*, ASCE, Reston, VA, USA, 44-53.

Runser, D., Fox, P.J., Bourdeau, P.L., 2001. Field performance of a 17 m-high reinforced soil retaining wall. *Geosynthetics International*, 8(5), 367-391.

Saghebfar, M., Abu-Farsakh, M., Ardah, A., Chen, Q., 2017. Performance monitoring of Geosynthetic Reinforced Soil Integrated Bridge System (GRS-IBS) in Louisiana. *Geotextiles and Geomembranes*, 45(2), 34-47.

Shen, P, Han, J., Zornberg, J., Morsy, A., Leshchinsky, D., Tanyu, B.F., Xu, C., 2019. Two and three-dimensional numerical analyses of geosynthetic-reinforced soil (GRS) piers. *Geotextiles and Geomembranes*, 47(3), 352-368.

Shen, P, Han, J., Zornberg, J., Tanyu, B.F., Christopher, B.R., Leshchinsky, D., 2020. Responses of geosynthetic-reinforced soil (GRS) abutments under bridge slab loading: Numerical investigation. *Computers and Geotechnics*, 123, 103566.

Talebi, M, Meehan, C.L., Leshchinsky D., 2017. Applied bearing pressure beneath a reinforced soil foundation used in a geosynthetic reinforced soil integrated bridge system. *Geotextiles and Geomembranes*, 45(6), 580-591.

Unified Facilities Guide Specifications (UFGS). (2008). *Section 35 31 19.20 – Articulating Concrete Block Revetments.*

Vieira, C.S., Lopes, M.L., Caldeira, L.M., 2013. Sand–geotextile interface characterisation through monotonic and cyclic direct shear tests. *Geosynthetics International*, 20(1), 26-38.

Wu, J.T.H., Ketchart, K., Adams, M., 2001. GRS bridge piers and abutments. *Report No. FHWA-RD-00-038*, U.S. DOT, Washington, D.C.

Wu, J.T.H., Lee, K.Z.Z., Helwany, S.B., Ketchart, K., 2006. Design and construction guidelines for geosynthetic-reinforced soil bridge abutments with a flexible facing. *NCHRP Report 556*, Transportation Research Board, Washington, D.C.

Xiao, C, Han, J., Zhang, Z., 2016. Experimental study on performance of geosynthetic-reinforced soil model walls on rigid foundations subjected to static footing loading. *Geotextiles and Geomembranes*, 44(1), 81-94.

Xu, C., Liang, C, Shen, P., 2019. Experimental and theoretical studies on the ultimate bearing capacity of geogrid-reinforced sand. *Geotextiles and Geomembranes*, 47(3), 417-428.

Yu, Y., Bathurst, R.J., Allen, T.M., 2016. Numerical modeling of the SR-18 geogrid reinforced modular block retaining walls. *Journal of Geotechnical and Geoenvironmental Engineering*, 142(5), 04016003.

Zheng, Y., Fox, P.J., 2016. Numerical investigation of geosynthetic-reinforced soil bridge abutments under static loading. *Journal of Geotechnical and Geoenvironmental Engineering*, 142(5), 07016032.

Zheng, Y., Fox, P.J., 2017. Numerical investigation of the geosynthetic reinforced soil-integrated bridge system under static loading. *Journal of Geotechnical and Geoenvironmental Engineering*, 143(6), 04017008.

Zheng, Y., Fox, P.J., McCartney, J.S., 2018a. Numerical simulation of deformation and failure behavior of geosynthetic reinforced soil bridge abutments. *Journal of Geotechnical and Geoenvironmental Engineering*, 144(7), 04018037.

Zheng, Y., Fox, P.J., McCartney, J.S., 2018b. Numerical simulation of deformation response of geosynthetic reinforced soil mini-piers. *Geosynthetics International*, 25(3), 271-286.

Zheng, Y., Sander, A.C., Rong, W., Fox, P.J., Shing, P.B., McCartney, J.S., 2018c. Shaking table test of a half-scale geosynthetic-reinforced soil bridge abutment. *Geotechnical Testing Journal*, 41(1), 171-192.

Zheng, Y., Fox, P.J., Shing, P.B., McCartney, J.S., 2019a. Physical model tests of half-scale geosynthetic reinforced soil bridge abutments. I: Static loading. *Journal of Geotechnical and Geoenvironmental Engineering*, 145(11). DOI: 10.1061/(ASCE)GT.1943-5606.0002158.

Zheng, Y., McCartney, J.S., Shing, P.B., Fox, P.J., 2019b. Physical model tests of half-scale geosynthetic reinforced soil bridge abutments. II: Dynamic loading. *Journal of Geotechnical and Geoenvironmental Engineering*, 145(11). DOI: 10.1061/(ASCE)GT.1943-5606.0002152.

Table 1. Soil parameters.

Property	Value
Unit weight, γ (kN/m^3)	17.7
Elastic modulus number, K	260
Unloading-reloading elastic modulus number, K_{ur}	312
Elastic modulus exponent, n	0.5
Failure ratio, R_f	0.65
Bulk modulus number, B	150
Bulk modulus exponent, m	0
Apparent cohesion, c' (kPa)	2.0
Friction angle, ϕ' (°)	51.3
Dilation angle, ψ (°)	13.0

Table 2. Interface parameters.

Property	Soil-geogrid [a]	Block-geogrid [b]	Soil-block Soil-bridge seat [c]	Block-block [d]	Bridge beam-bridge seat [e]
Friction angle, δ_i'	46.7°	35.0°	39.1°	36.0°	21.8°
Adhesion, c_i'	1.7 kN/m/m	0	1.3 kPa	0	0
Normal stiffness, k_n	-	-	100GPa/m	100GPa/m	100GPa/m
Shear stiffness, k_s	4MPa/m	400MPa/m	400MPa/m	400MPa/m	400MPa/m

[a] Based on average of data (RF_i = 0.85) from Vieira et al. (2013)

[b] Based on data reported by Unified Facilities Guide Specifications (2008).

[c] Based on data (RF_i = 0.65) from Ling et al. (2010)

[d] Based on data reported by Yu et al. (2016)

[e] Based on coefficient of friction of 0.4 for elastomeric bearing pad suggested by California Department of Transportation (1994)

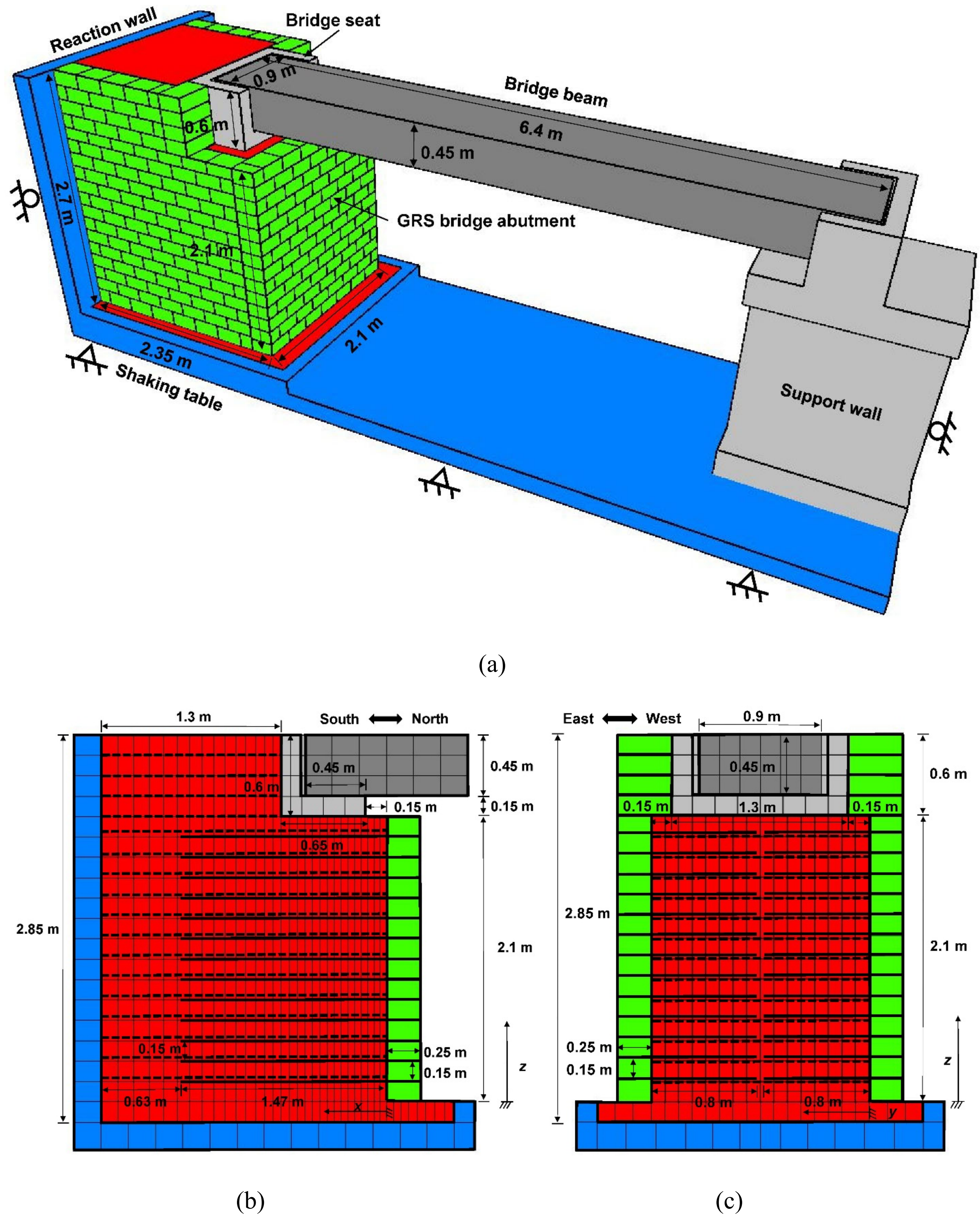

Figure 1. 3D numerical model for GRS bridge abutment: (a) model configuration; (b) longitudinal cross-section; (c) transverse cross-section.

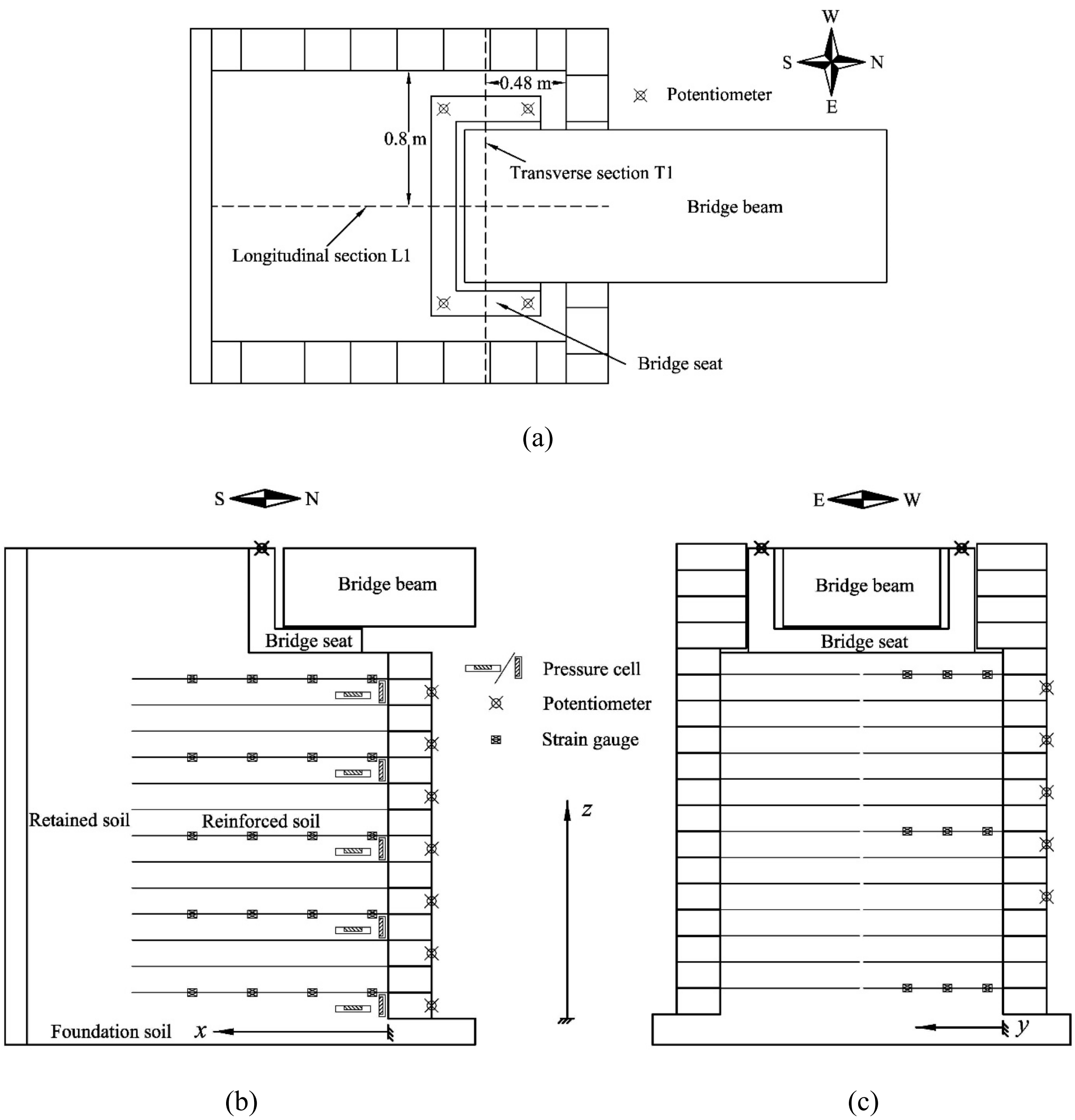

Figure 2. Instrumentation for GRS bridge abutment: (a) top view; (b) longitudinal section L1 (y = 0.8 m); (c) transverse section T1 (x = 0.48 m) (after Zheng et al. 2019a).

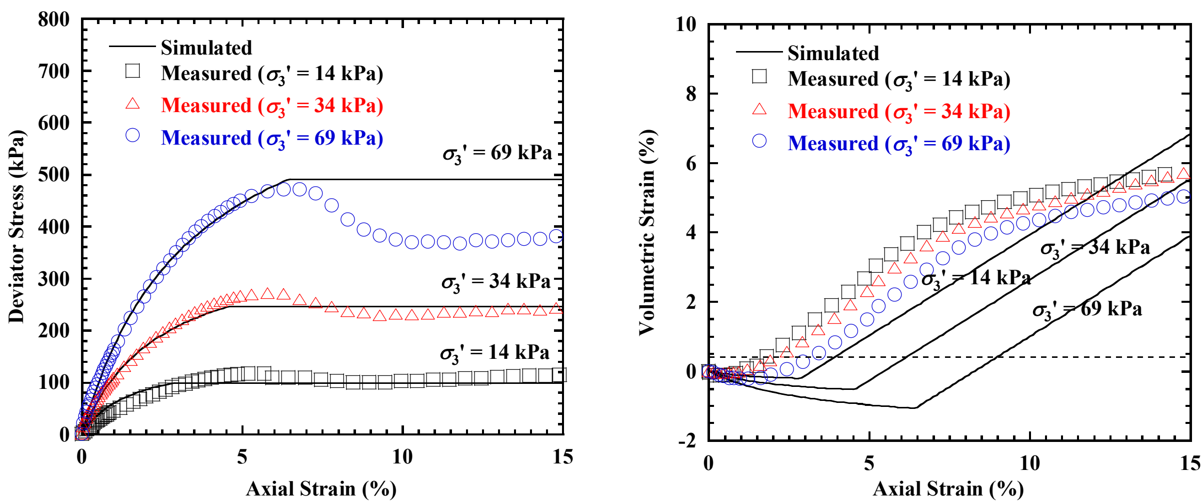

(a) (b)

Figure 3. Triaxial compression test results: (a) deviator stress vs. axial strain; (b) volumetric strain vs. axial strain.

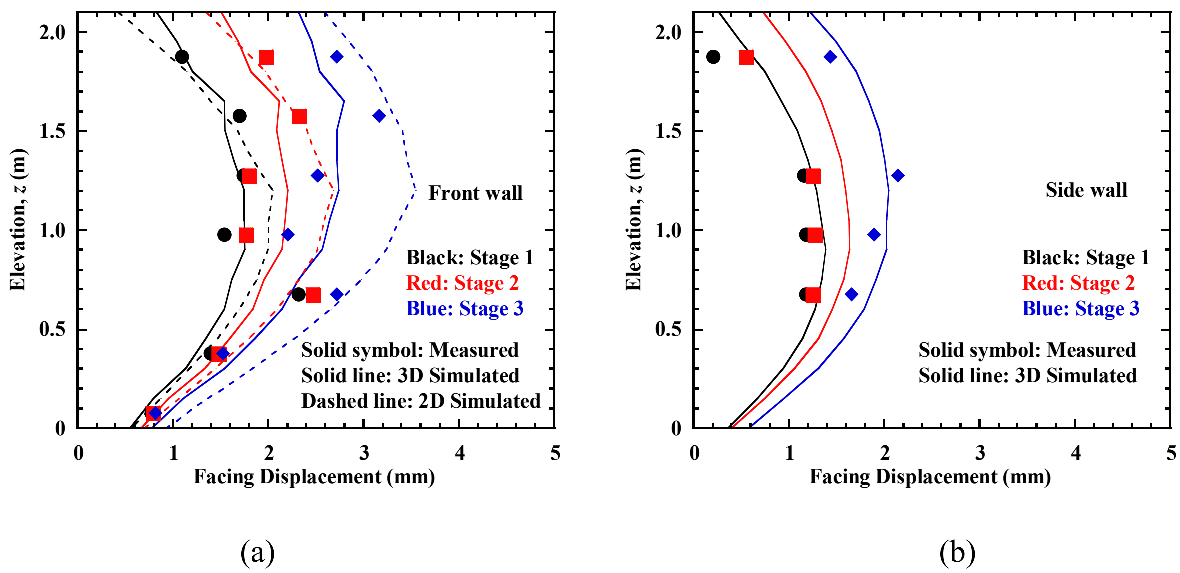

Figure 4. Profiles of facing displacement: (a) longitudinal section; (b) transverse section.

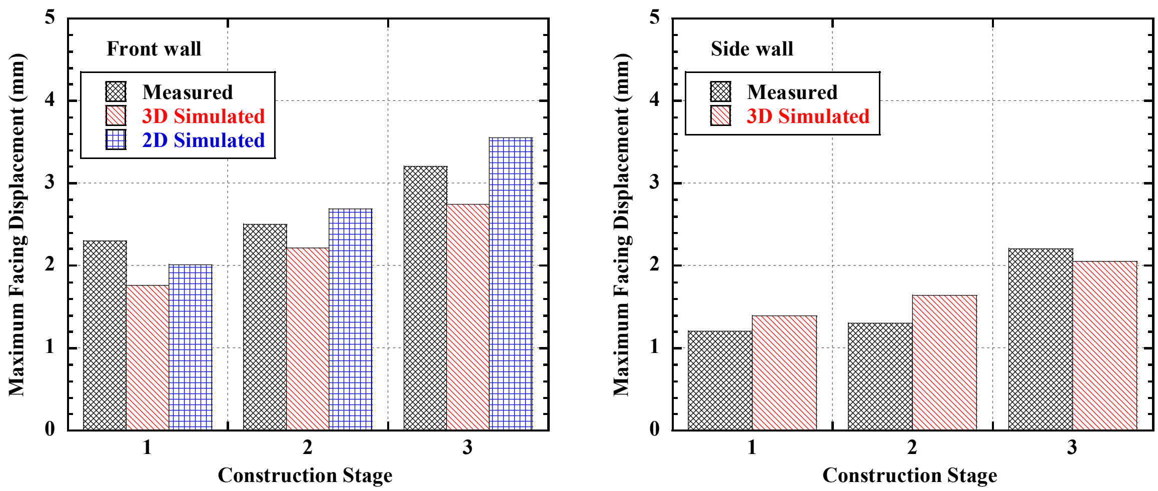

(a) (b)

Figure 5. Maximum facing displacement: (a) longitudinal section; (b) transverse section.

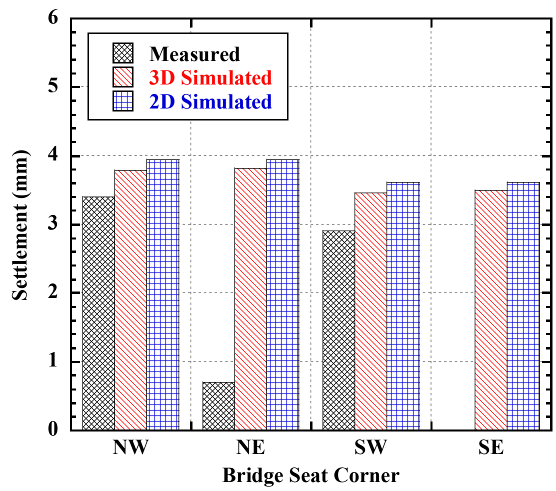

Figure 6. Settlement at the top corners of the bridge seat.

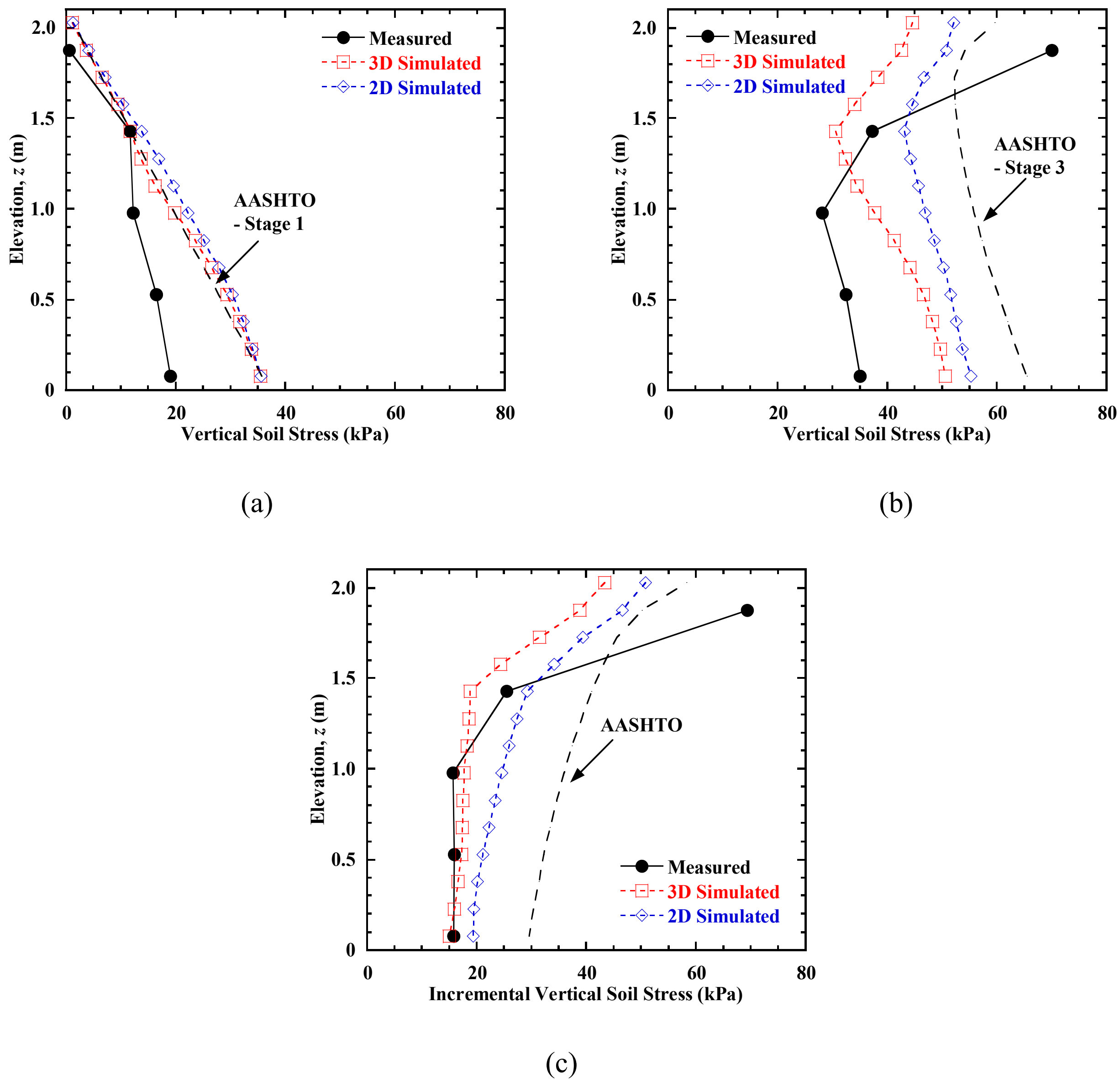

Figure 7. Profiles of vertical soil stress under bridge seat for longitudinal section: (a) Stage 1; (b) Stage 3; (c) Incremental from Stage 1 to Stage 3.

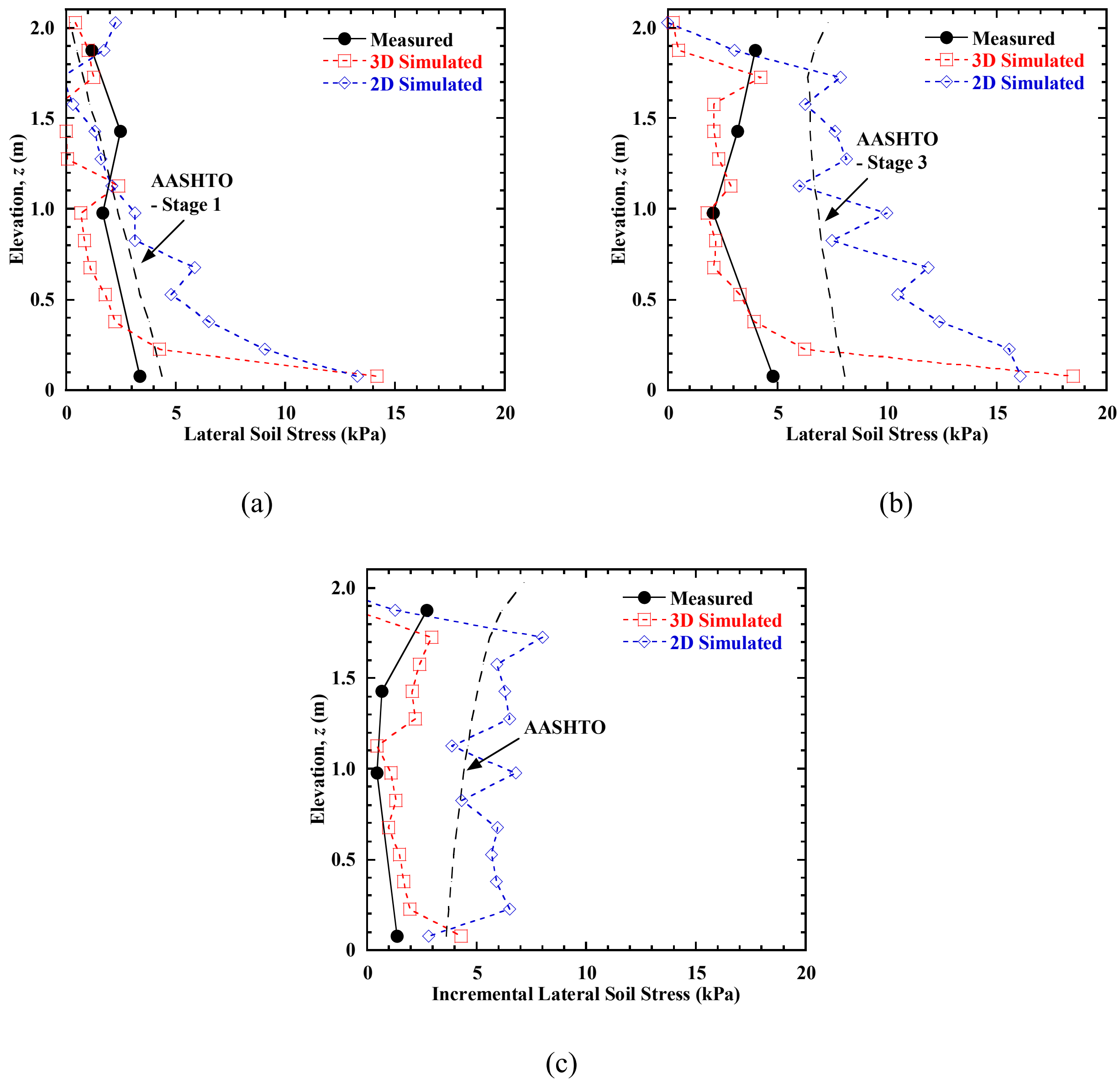

Figure 8. Profiles of lateral soil stress behind front wall facing for longitudinal section: (a) Stage 1; (b) Stage 3; (c) Incremental from Stage 1 to Stage 3.

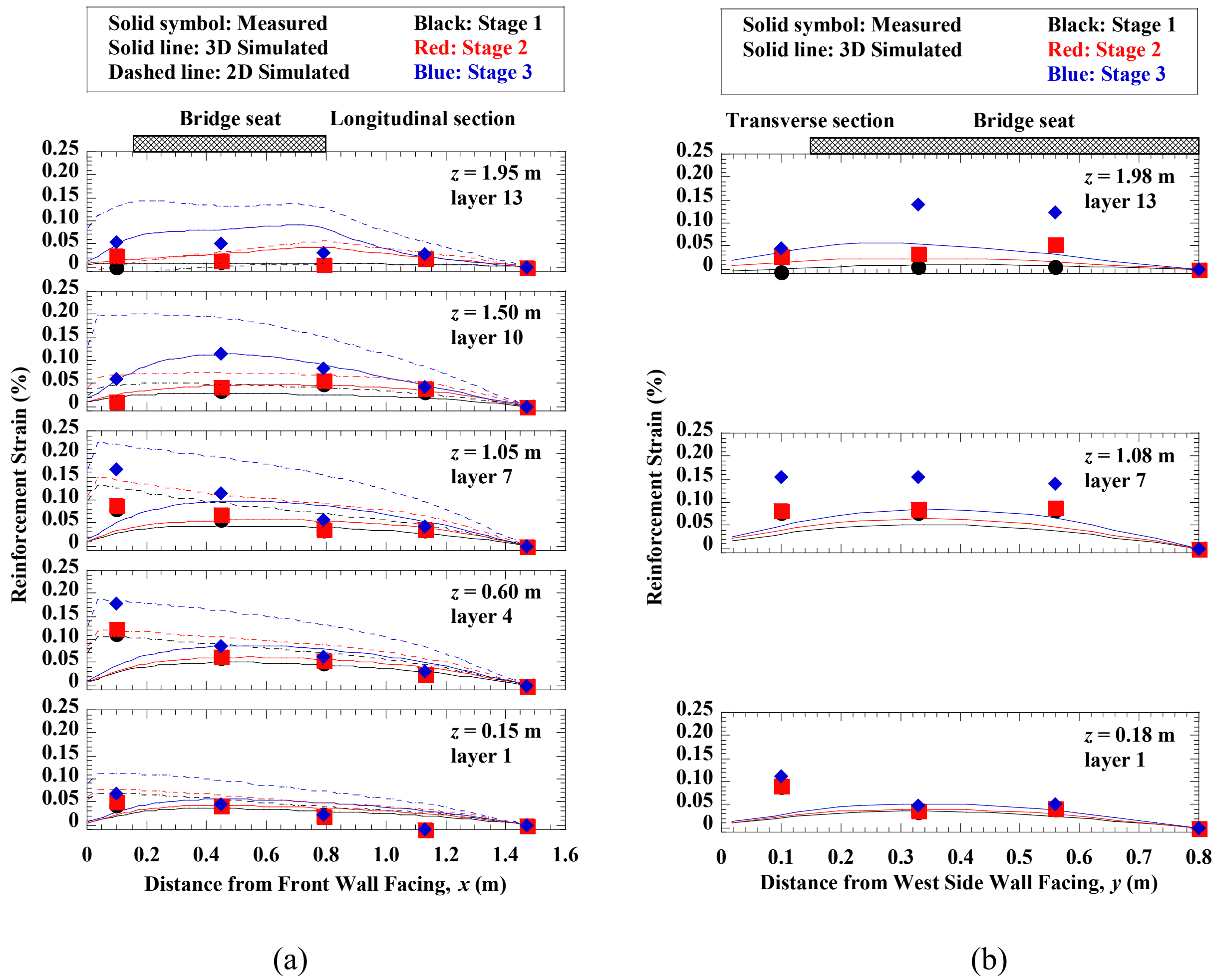

Figure 9. Distributions of tensile strain in reinforcement layers: (a) longitudinal section; (b) transverse section.

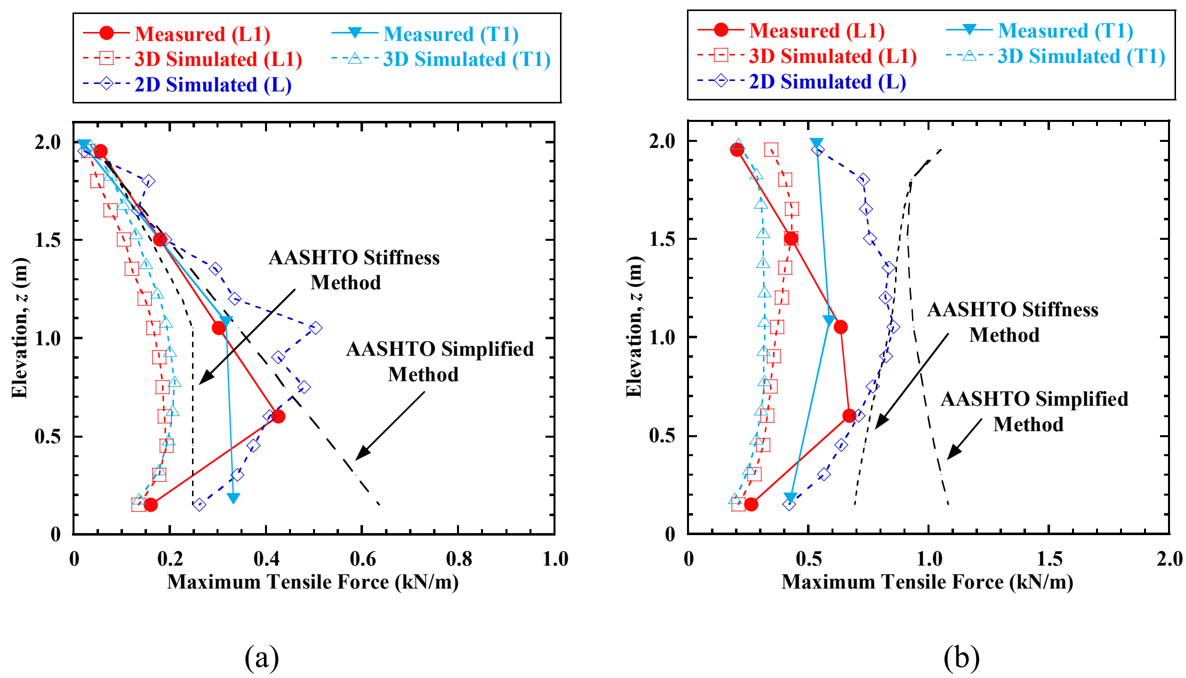

Figure 10. Profiles of maximum tensile force in reinforcement layers: (a) Stage 1; (b) Stage 3.